Article

Not peer-reviewed version

On the Energy Dependence of the PL of RE Ions in LuBO3:RE (RE = Ce, Eu, Gd, or Tb)

Franziska Schröder , Sven Reetz * , Thomas Jüstel *

Posted Date: 7 March 2024

doi: 10.20944/preprints202403.0444.v1

Keywords: Energy dependent photoluminescence; ortho-borates; scintillation

Article

On the Energy Dependence of the PL of RE Ions in $LuBO_3$:RE (RE = Ce, Eu, Gd, or Tb)

Franziska Schröder, Sven Reetz * and Thomas Jüstel *

Department of Chemical Engineering, FH Münster University of Applied Sciences, Stegerwaldstraße 39, D-48565 Steinfurt, Germany

* Correspondence: sven.reetz@fh-muenster.de (S.R.); tj@fh-muenster.de (T.J.)

Abstract: $LuBO_3$ crystallizes in the calcite type ($CaCO_3$) structure and is a widely applied inorganic host for luminescent materials and scintillators. Even though many scientific works have been published concerning the optical properties of rare earth doped $LuBO_3$, so far, no study of the emission spectra as function of the excitation energy of such orthoborates has been conducted. Therefore, this work deals with the photoluminescence of RE doped $LuBO_3$ with RE = Ce^{3+}, Eu^{3+}, Gd^{3+}, or Tb^{3+}, while an emphasize is laid on the energy dependence of these four luminescent compounds.

Keywords: energy dependent photoluminescence; ortho-borates; scintillation

1. Introduction

For many decades, rare earth orthoborates $REBO_3$ have been of tremendous scientific interest due to their outstanding optical properties. They exhibit, e.g. a rather large optical band gap and are thus transparent down to the vacuum ultraviolet (VUV) range. Moreover, they display a large optical damage threshold and high luminescence efficiency for the dopants Ce^{3+}, Eu^{3+}, Gd^{3+}, and Tb^{3+}. Hence, they were frequently used for various practical applications, like in gas discharge lamps, radiation detectors, and plasma display panels [1–3].

One important member of the rare earth ortho-borates is $LuBO_3$ due to its excellent scintillating properties [4,5]. $LuBO_3$ can crystalize in the calcite structure ($R\bar{3}c$), or vaterite structure ($P6_3/mmc$) if it is heated above 1310 °C [6]. Trivalent cations are octahedrally coordinated in both structures, and an additional 12-coordinated site is available in the vaterite structure [7]. The symmetry of the cation environment decreases accordingly with the phase change [8]. Therefore, researchers have investigated different synthesis methods, such as solid-state reaction, sol-gel method or hydrothermal approach, to yield the desired crystal structure, particle size, and morphology [9]. Despite these efforts and the relevance of $LuBO_3$ as a host lattice for optical materials, the photoluminescence of various $LuBO_3:RE^{3+}$ were not systematically studied. This paper coherently presents, to the best of our knowledge, the excitation, emission, X-ray-excited emission, energy-dependent emission, and temperature-dependent emission properties of $LuBO_3:RE^{3+}$ with RE = Ce^{3+}, Eu^{3+}, Gd^{3+}, Tb^{3+} for the first time.

2. Experimental Section

A series of several microscale powder samples of the compound $LuBO_3$, substituted with 1% each of Ce, Eu, Gd, and Tb, were prepared by the solid-state method. For this purpose, stoichiometric amounts of Lu_2O_3 (Treibacher 99.9%) and, depending on the activator ion used, CeO_2 (Treibacher 99.9%), Eu_2O_3 (Treibacher 99.9%), Gd_2O_3 (Treibacher 99.9%) and Tb_4O_7 (Treibacher 99.9%) were weighed in. In addition, H_3BO_3 (Merck) was added to the solid solution with an excess of 20%.

 doi:10.20944/preprints202403.0444.v1

The precursors were thoroughly mixed in a mortar with acetone and then homogenized. After the acetone has completely evaporated, the reactant mixture was transferred to a corundum crucible and calcined at 1200 °C for 12 hours.

The reaction atmosphere was adjusted to the corresponding activator ions. Eu^{3+}, Gd^{3+}, and Tb^{3+} were heated in air, while the Ce^{3+} doped borate was heated under CO to ensure that such oxidation sensitive trivalent ion is not oxidized. After the heating step, the products were again thoroughly triturated in a mortar.

3. Analytical Measurements

3.1. Determination of the Phase Purity

Powder X-ray diffraction (PXRD) patterns were recorded for each sample with a Rigaku Miniflex II diffractometer. The measurement geometry corresponds to the Bragg-Brentano geometry using a Cu K_α radiation source with an electrical input power of 450 W. Diffractograms were recorded between 2θ = 10-80° with a step width of 0.02°.

3.2. Particle Size Distribution

The particle size distributions were characterized via laser scattering (λ_1 = 405 nm, λ_2 = 650 nm). The measurements were performed with the partica LA-950V2 (HORIBA)laser scattering particle size distribution analyzer.

3.3. Reflection Spectroscopy

Diffuse reflectance spectra were recorded on an Edinburgh Instruments FLS920 spectrometer with an integration sphere coated by Spectralon®, an ozone-free Xe-arc lamp (450 W) and a single photon counting photomultiplier (Hamamatsu, R298), which was cooled to 253 K. The white powder standard used was optical grade $BaSO_4$ (Sigma Aldrich, 99.99 %).

3.4. Photoluminescence Studies

Photoluminescence spectra for VUV excitation were performed with a fluorescence spectrometer based on a modified Edinburgh Instrument FLS 920. The standard UV/VIS excitation arm was exchanged by a VUV excitation arm. Which was equipped with a D_2 lamp (DS-775) as the excitation source, a VM-504 VUV monochromator (Acton research) and a focusing device which was mirror-based. The monochromator is equipped with 1200 grooves per mm (F/mm) and manually adjustable (micrometer screw) inputs and outputs. The internal volume of the monochromator and focusing unit is under vacuum ($<5*10^{-5}$ mbar) created by an attached turbopump. The D_2 lamp emits directly into the vacuum path through an MgF_2 window. The sample is measured with a modified sample holder at a 45° angle to the excitation beam. Measurements were therefore performed at 90°.

Measurements under X-ray excitation were performed using an Edinburgh Instruments FLS 980 fluorescence spectrometer. The spectrometer is equipped with a photomultiplier R 298P (Hamamatsu) cooled to 253 K by a Peltier element. An Oxford Instruments Neptune 5200 X-ray tube with an operating voltage range of 10-50 kV was used as the excitation source.

4. Results and Discussion

4.1. X-ray Diffraction Studies

The present microscale $LuBO_3$ samples belong to the orthoborates and thus crystallize in a trigonal crystal system with space group $R\bar{3}c$ (#167) [1].

The unit cell has a volume of 0.33899 nm^3, where a = b = 0.4914(13) nm and c = 1.621(7) nm. It comprises six formula units and therefore 30 atoms. Each atomic species occupies one layer. Figure 1 shows a schematic representation of the unit cell and the arrangement of the polyhedra. The lutetium atoms are coordinated six-fold to an octahedron (in blue) and the boron atoms are coordinated

 doi:10.20944/preprints202403.0444.v1

threefold to a coplanar triangle (in green). Each oxygen atom of the BO_3 polyhedron is corner-linked to a LuO_6 polyhedron [1].

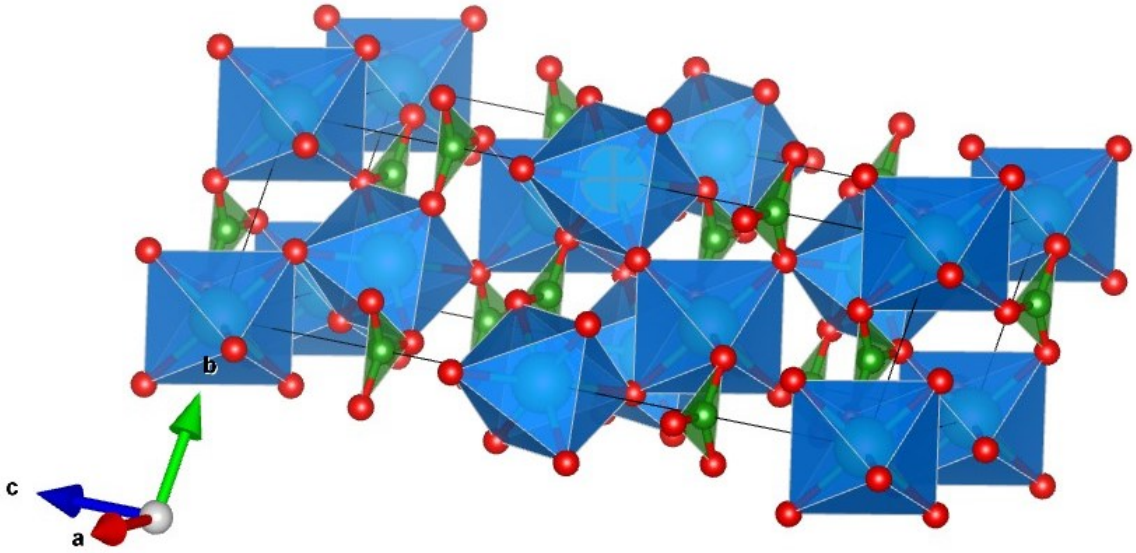

Figure 1. Schematic representation of the $LuBO_3$ unit cell modified after [1]. The LuO_6 polyhedra (in blue) form an octahedron and the BO_3 polyhedra (in green) form a coplanar triangle [1]. (color should be use.d).

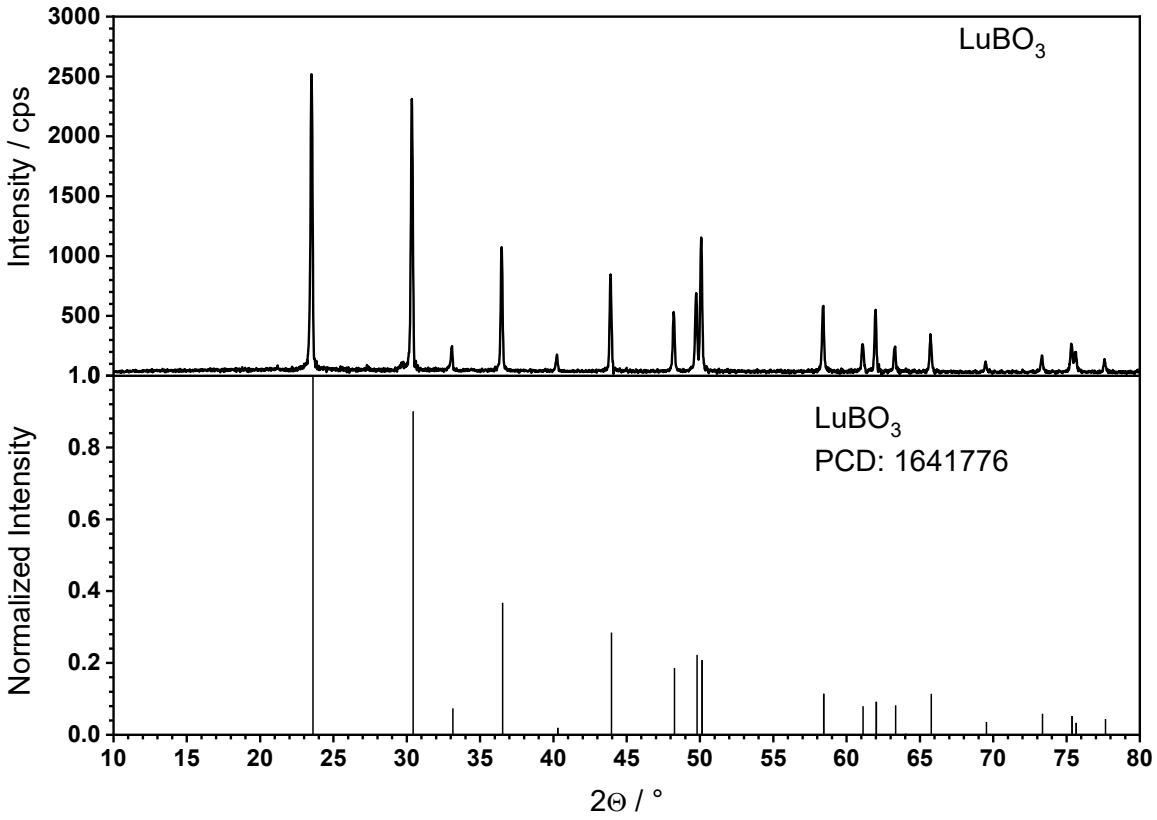

Figure 2. X-Ray diffraction patterns of the as-prepared undoped $LuBO_3$ sample compared to the reference pattern.

 doi:10.20944/preprints202403.0444.v1

The recorded powder diffractograms of the other samples are also in line with the reference data from literature, so that it is assumed that the samples are single phase. The results are shown in Figure 3. Columns a-d show the x-ray patterns of as-synthesized powder samples with the indicated activators, respectively. The reference PCD 1641776 from the literature is shown in the bottom row e.

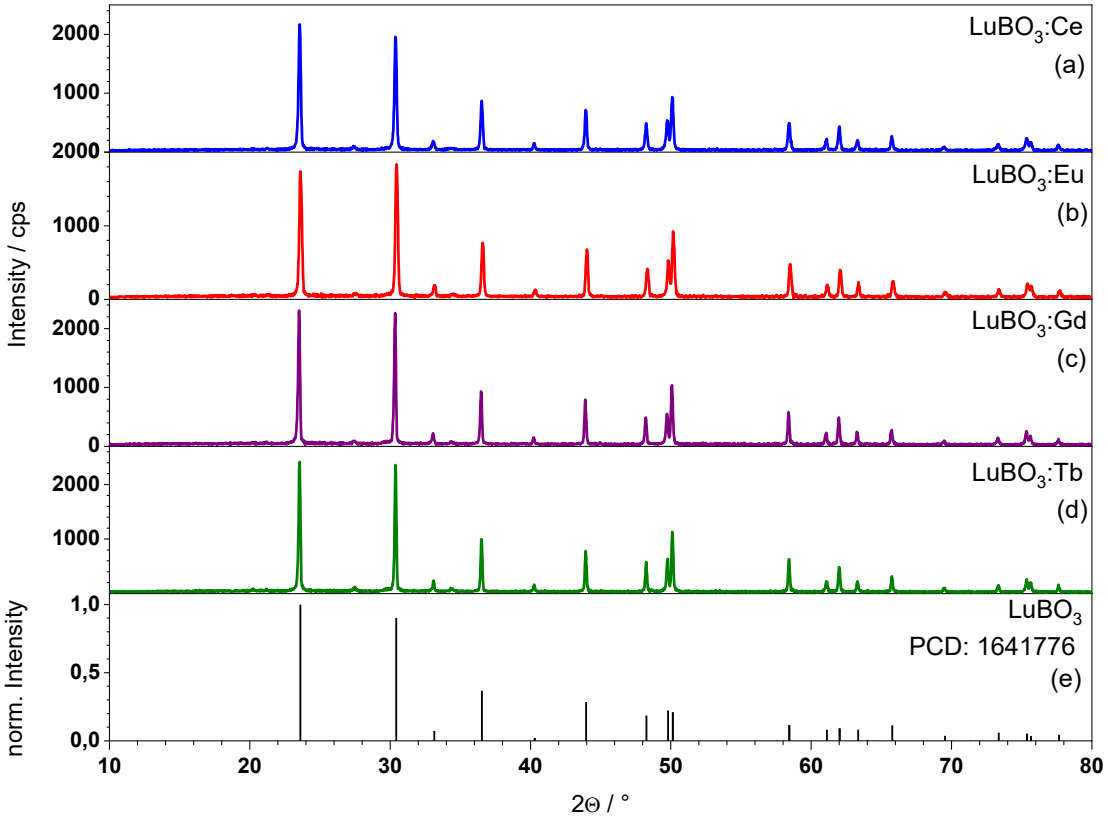

Figure 3. X-Ray diffraction patterns of the as-prepared $LuBO_3:RE^{3+}$ (RE = Ce^{3+}, Eu^{3+}, Gd^{3+}, Tb^{3+}) µ-scale powder samples.

4.2. Particle Size Distribution

The particle size distribution measurements were conducted for all samples. The particle size of the prepared $LuBO_3:Ce^{3+}$ sample is representatively shown in Figure 4. The sample is unimodally distributed but shows tailing due to the presence of bigger particles. This broadening of the distribution leads to a high D_{90} values.

Preprints.org (www.preprints.org) | NOT PEER-REVIEWED | Posted: 7 March 2024 doi:10.20944/preprints202403.0444.v1

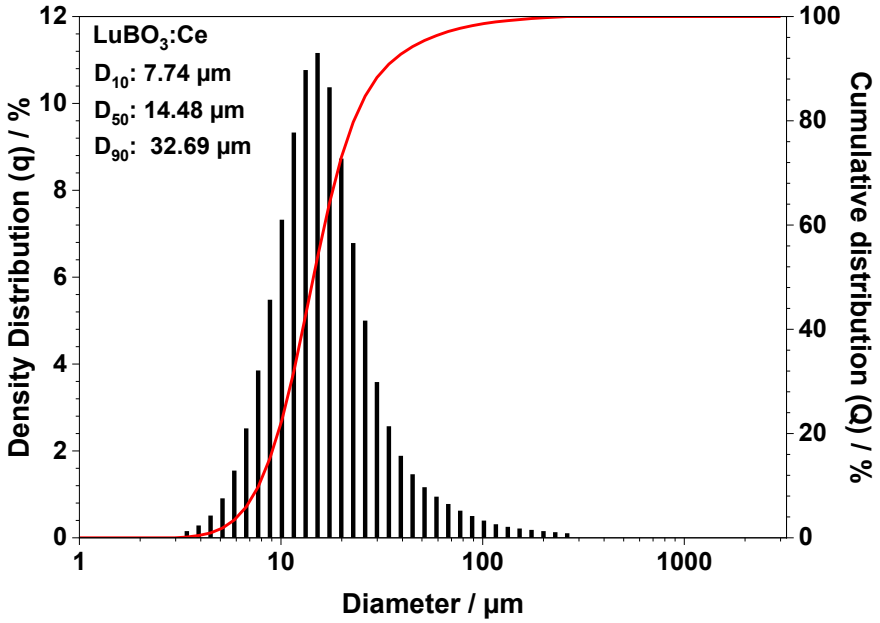

Figure 4. Particle size distribution of $LuBO_3:Ce^{3+}$ which is representative for the particle size distributions of all samples investigated in this work.

Similar distributions were observed for the other samples. Furthermore, the D_{10} and D_{50} values are similar, whereas the D_{90} values vary significantly (see Table 1).

Table 1. Measured particle size distribution D_{10}, D_{50} and D_{90} of the prepared microscale phosphor samples.

Sample	D_{10} / µm	D_{50} / µm	D_{90} / µm
$LuBO_3$	7.35	14.38	70.06
$LuBO_3:Ce^{3+}$	7.74	14.48	32.69
$LuBO_3:Eu^{3+}$	7.18	14.10	51.76
$LuBO_3:Gd^{3+}$	8.11	17.61	119.21
$LuBO_3:Tb^{3+}$	8.34	17.12	63.50

4.3. Reflection Spectra

Undoped $LuBO_3$ show a very high reflectance between 350 and 800 nm, which causes the pure white body color (Figure 5). Below 350 a weak absorption band appears, which might be caused by defect centers (Urbach tailing), since the band gap of $LuBO_3$ is about 6.4 eV [10].

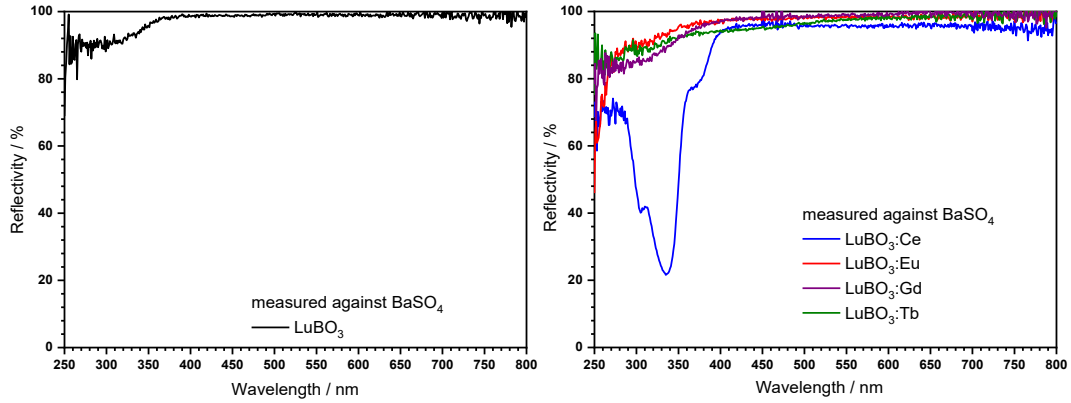

Figure 5. Reflection spectra of the as-prepared $LuBO_3$ samples. Undoped $LuBO_3$ (left image) and substituted with 1% of Ce, Eu, Gd, or Tb as activators (right image). (color should be used).

Preprints.org (www.preprints.org) | NOT PEER-REVIEWED | Posted: 7 March 2024 doi:10.20944/preprints202403.0444.v1

The reflectance spectrum of the Ce^{3+} comprising microscale sample (blue line) shows a strong absorption feature which is observed in the range between 280 and 410 nm. The minimal reflectance is around 303 and 335 nm with a shoulder at 376 nm. This composition exhibits a high reflectivity of almost 100% between 400 and 800 nm. The Eu-doped sample shows a sharp increase at 250 nm due to the ligand-to-metal charge transfer, which starts steadily decreasing at roughly 280 nm. Beyond this, the material exhibits a strong reflectance, and no absorption bands or lines are observed. Finally, the Gd^{3+}- and Tb^{3+}-substituted sample do not absorb in the investigated spectral range. There are no absorptions in the spectra that might be attributed to absorption by Tb^{3+}, other rare earths or impurities. The measurements are consistent with the white body color of the samples.

4.4. Photoluminescence Spectroscopy

4.4.1. $LuBO_3:Ce^{3+}$

In addition to the reflectance, an excitation spectrum (red spectrum) was recorded between 120 and 350 nm with a fixed emission wavelength of 362 nm, which is depicted in Figure 6. This spectrum shows a band between 295 and 350 nm with two maxima around 303 and 335 nm which are assigned to the transitions from the spin-orbit split ground state level $^7F_{5/2}$ and $^7F_{7/2}$ to the lowest crystal-field component of the $5d^1$ configuration of Ce^{3+} [2,3].

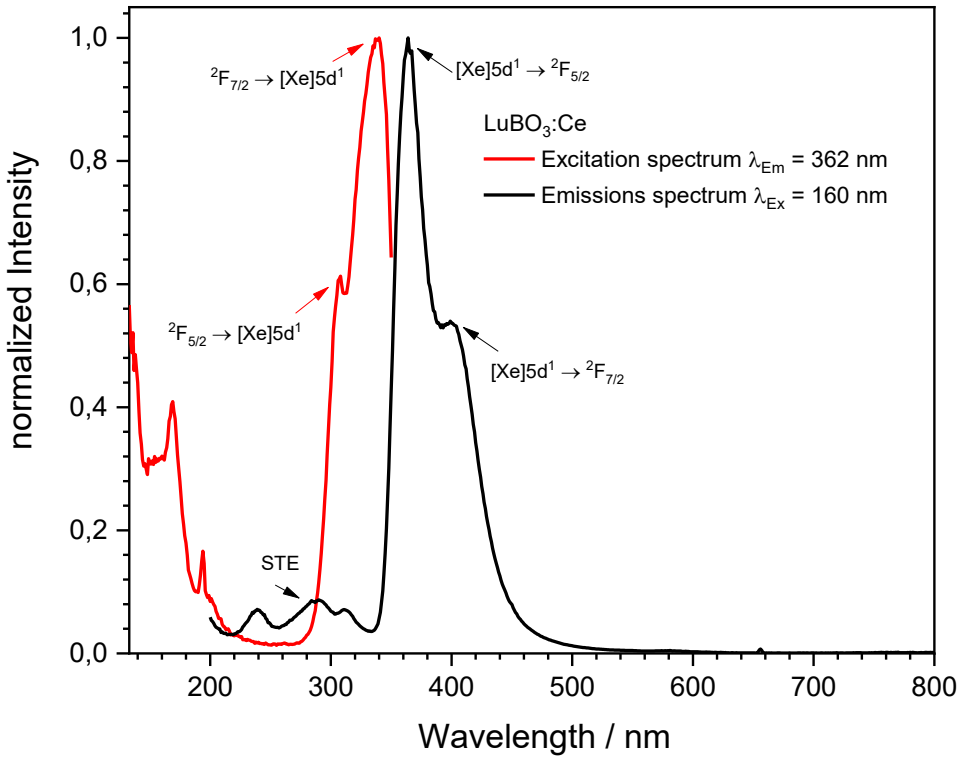

Figure 6. Excitation (red) and emission (black) spectra of Ce^{3+} doped $LuBO_3$.

The position of the excitation maxima agrees quite well with the position of the absorption bands of the reflection measurement.

An excitation maximum around 167 nm is observed, thus at the high energy edge to the band between 295 and 350 nm. This excitation band can be attributed to a band-to-band transition, since the band gap of the material is approximately 6.4 eV (194 nm) [10].

Furthermore, an emission spectrum was recorded under an excitation wavelength of 160 nm between 200 and 800 nm. The result is shown as the black curve in Figure 6.

A broad emission pattern with three maxima around 240, 288 and 311 nm can be recognized between 200 and 250 which is probably due to recombination processes of self-trapped excitons (STE)

 doi:10.20944/preprints202403.0444.v1

[2]. Furthermore, a broad emission band with two maxima between 350 and 550 nm can be observed. The maxima are around 363 nm and 401 nm. The maxima around 363 nm shows the highest relative emission intensity and is due to a transition from the lowest crystal-field component of the [Xd]$5d^1$ configuration to the ground state $^2F_{5/2}$. The maxima around 401 nm is due to the transition from the 5d-band to $^2F_{7/2}$ [2,3,10,11]. Between 500 and 800 nm, there are no further emission bands or lines detectable.

The CIE1931 chromaticity coordinates (x, y) were calculated for $LuBO_3:Ce^{3+}$ emission in the violet spectral range, the. The calculation results in a luminous efficacy of 8 lm/W_{vis} and the color coordinates are x = 0.1691 and y = 0.0397 (see Figure 7).

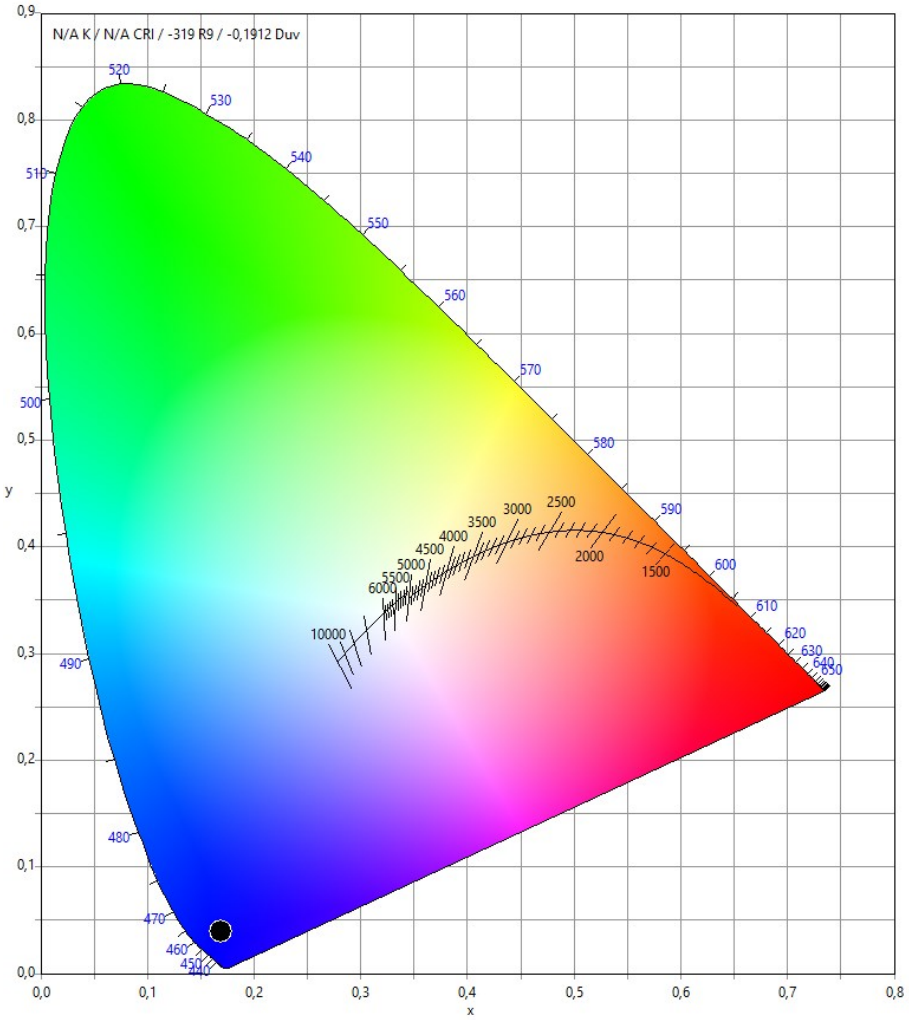

Figure 7. CIE1931 color chart with the x, y color point of $LuBO_3:Ce^{3+}$ (color should be used).

4.4.2. $LuBO_3:Eu^{3+}$

The excitation spectrum shows a charge transfer occurring in the VUV and UV-C range (see Figure 8), which can be attributed to the transfer of electron density from 2p orbitals of O^{2-} to europium´s 4f orbitals. Strong emission lines were observed at 587 nm and 589 nm. These correspond to the $^5D_0 \rightarrow {}^7F_1$ transition, which is significantly split due to the calcite symmetry of the host lattice. The additional present 4f-4f transitions indicate deviations from the S_6 symmetry of the Eu^{3+} ions allowing electric dipole transitions according to the parity transition rules [8,9]. The broad emission band at 300 nm is likely related to defect-related fluorescence phenomena.

Preprints.org (www.preprints.org) | NOT PEER-REVIEWED | Posted: 7 March 2024 doi:10.20944/preprints202403.0444.v1

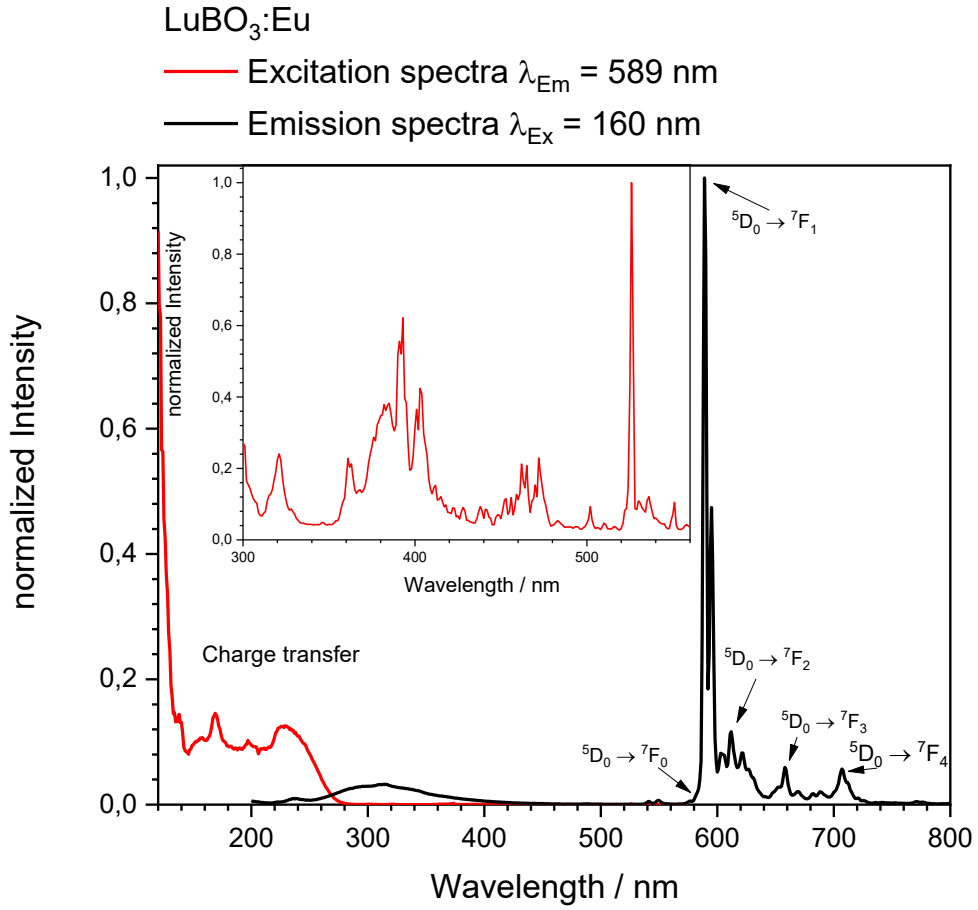

Figure 8. Excitation (red) and emission (black) spectra of Eu^{3+} doped $LuBO_3$.

Since $LuBO_3$:Eu show orange emission in the visible spectral range, the CIE1931 chromaticity coordinates (x, y) were calculated. The calculation results in a luminous efficacy of 342 lm/W_{vis} and the color coordinates are x = 0.5910 and y = 0.3907 (see Figure 9).

Preprints.org (www.preprints.org) | NOT PEER-REVIEWED | Posted: 7 March 2024 doi:10.20944/preprints202403.0444.v1

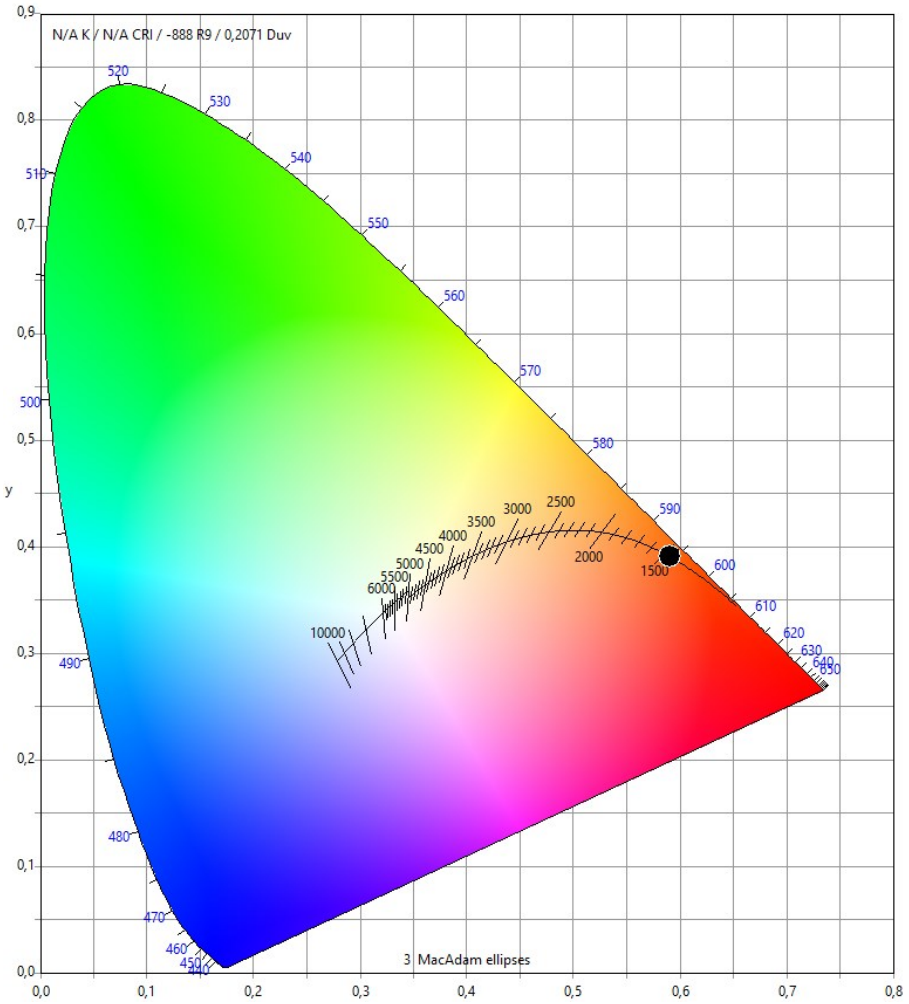

Figure 9. CIE1931 color chart with the x, y color point of $LuBO_3:Eu^{3+}$ (color should be used).

4.4.3. $LuBO_3:Gd^{3+}$

The excitation spectrum shows a peak at 175 nm with a very steep low energy edge. This excitation corresponds to the band excitation of the host matrix, and thus fits rather well to the optical band gap of $LuBO_3$. A single sharp emission line is observed at 312 nm, which can be assigned to the $^6P_{7/2} \rightarrow {}^8S_{7/2}$ transition. This line overlaps with a broad emission band that is assigned to an STE emission due to defects in the material (see Figure 10).

 doi:10.20944/preprints202403.0444.v1

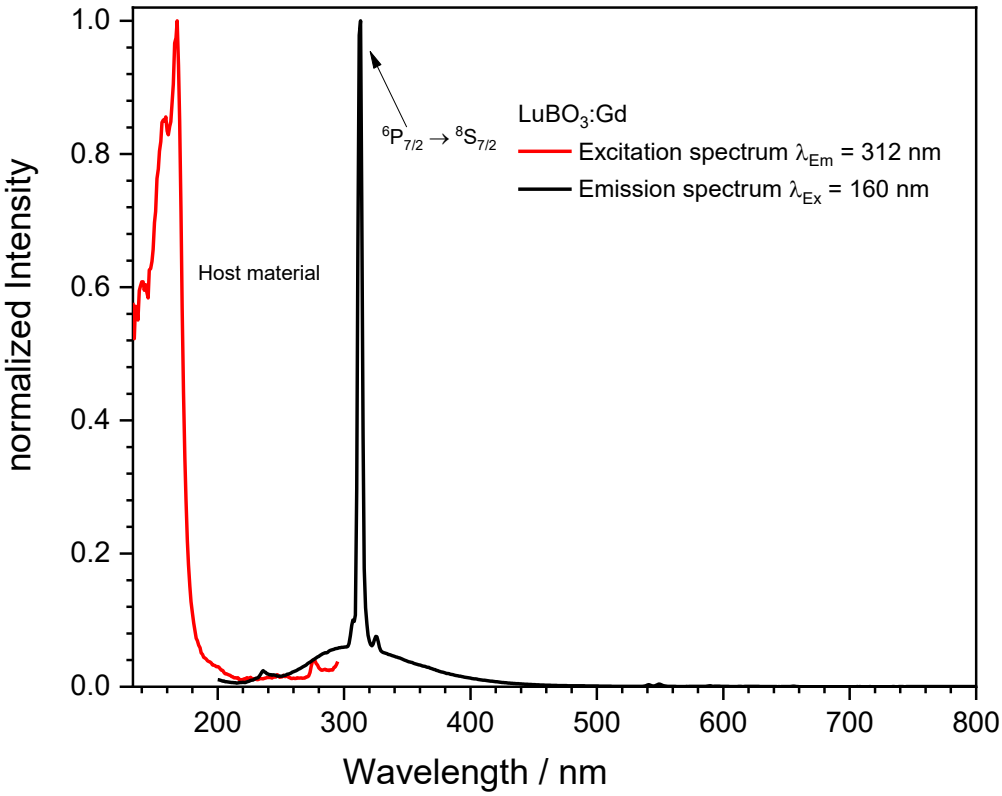

Figure 10. Excitation (red) and emission (black) spectra of the sample $LuBO_3:Gd^{3+}$.

4.4.4. $LuBO_3:Tb^{3+}$

The lutetium orthoborate terbium was also optically characterized in terms of excitation and emission behavior. The results are shown in Figure 11.

Preprints.org (www.preprints.org) | NOT PEER-REVIEWED | Posted: 7 March 2024 doi:10.20944/preprints202403.0444.v1

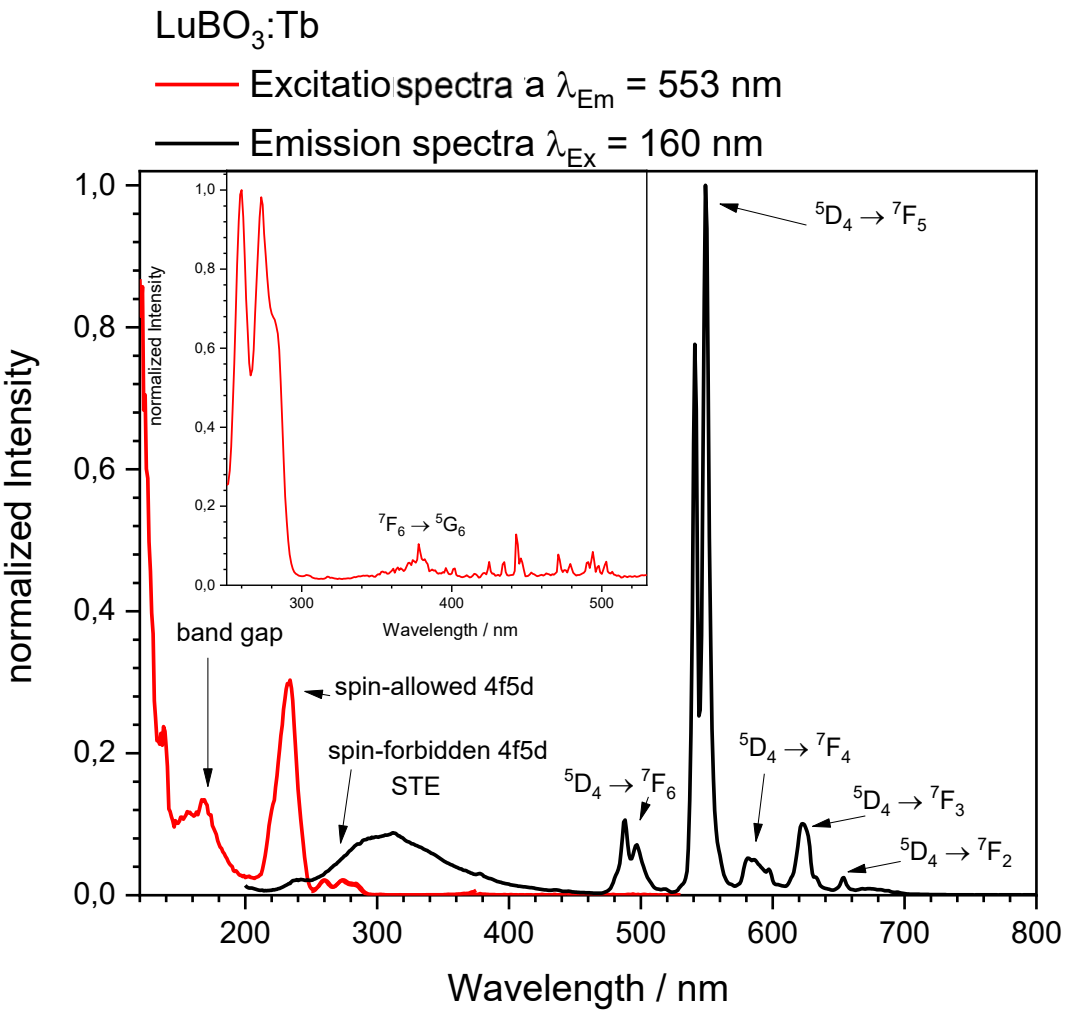

Figure 11. Excitation (red line) and emission (black line) spectra of the Tb^{3+} doped $LuBO_3$ sample.

The excitation spectrum was monitored for the Tb^{3+} emission at 553 nm and is shown as a red line. Two excitation maxima are observed between 250 and 300 nm. The first band is located at 261 nm and the second one at 274 nm with a shoulder at 283 nm. In addition, minor signals are found between 300 and 550 nm. The bands between 250 and 300 nm are presumably due to a transition from the $[Xe]4f^8$ ground state configuration to the $[Xe]4f^75d^1$ excited state configuration, which are assigned as spin-forbidden 4d5d transitions. These are split in local S_6 symmetry to three crystal-field components [12]. Another strong band at 230 nm is observed, which is assigned as the spin-allowed 4f5d transition. The energetic splitting results from the high-spin ^9D_J and the low-spin ^7D_J configurations, respectively [13,14]. On the basis of Hund's rule, the energetically higher maximum can be traced back to the transition to the low-spin configuration.

Since the transition to the low-spin configuration ($^7F_J \rightarrow {}^7D$) is spin allowed in contrast to the high-spin variant ($^7F_J \rightarrow {}^9D$), it was assumed that the intensity of the signal for the transition to the low-spin configuration is more intense than that of the signal representing the transition to the high-spin configuration. In contrast to the signals between 200 and 300 nm, the peaks between 300 and 500 nm are 4f → 4f transitions which are parity forbidden in contrast to the 4f5d transitions, which explains the difference in intensity.

The emission spectrum is shown in black and was recorded at a fixed excitation wavelength of 160 nm between 200 and 800 nm. A broad band can be seen between 200 and 450 nm, which is due to STE Luminescence [2]. Between 450 and 800 nm, bands with narrow maxima are seen that are due to the 4f → 4f transitions within the Tb^{3+}. The maximum around 487 nm is due to the transition out of the $^5D_4 \rightarrow {}^7F_6$, and the one around 546 nm is due to the transition between the $^5D_4 \rightarrow {}^7F_5$ states. The

 doi:10.20944/preprints202403.0444.v1

signal around 582 nm is due to the transition $^5D_4 \rightarrow {}^7F_4$ and the signal around 622 nm can be linked to the transition between the levels $^4D_5 \rightarrow {}^7F_3$.

A comparison of the recorded spectra with previously published spectra shows that they are in good agreement with previously published results [13–16]. As with $LuBO_3:Eu^{3+}$, the emission from the $LuBO_3:Tb^{3+}$ phosphor sample is within the visible spectral range, so the luminous efficacy and CIE1931 chromaticity coordinates (x, y) were calculated (Figure 12). The calculation resulted in a luminous efficacy of 473 lm/W_{vis} and the coordinates are x = 0.3188 and y = 0.6030.

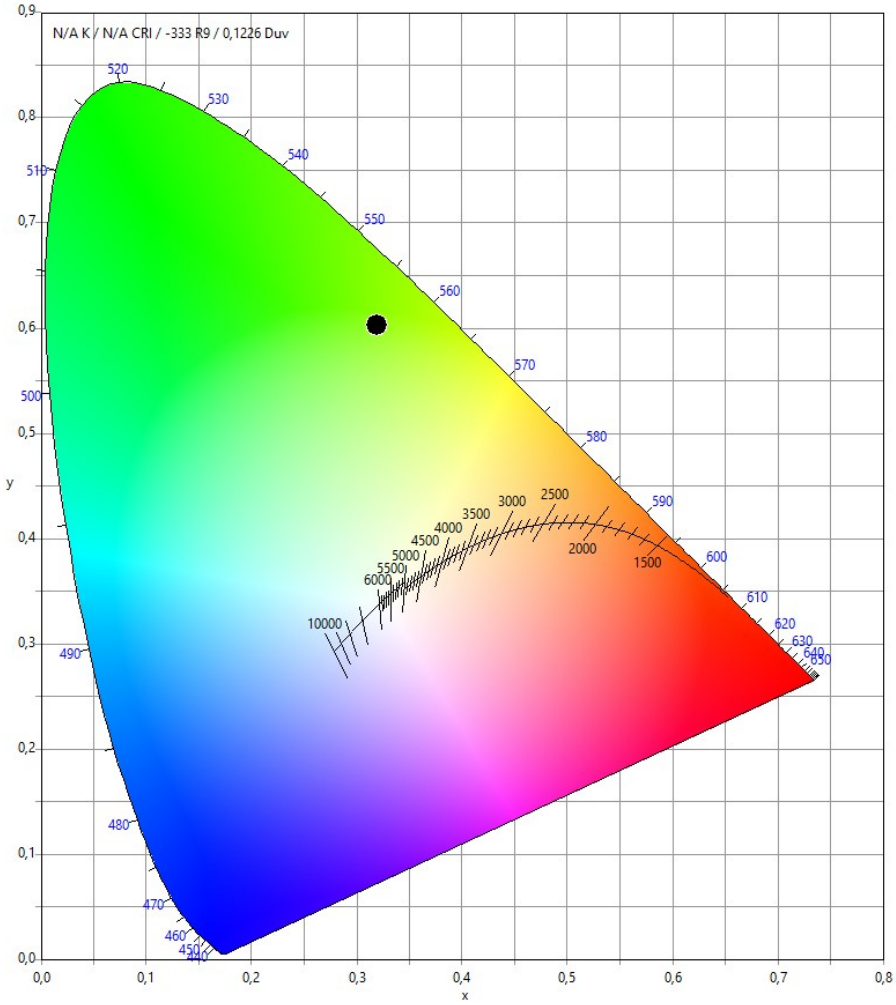

Figure 12. CIE diagram of $LuBO_3:Tb^{3+}$ (color should be used).

4.5. X-Ray Excited Emission Spectra

In addition to the fluorescence spectra, X-ray excited emission spectroscopy (XES) spectra were recorded for the presented samples. Thereby, all luminescent species are excited, which includes low laying bands that are not excited with classical excitation sources. The measurements were conducted with a voltage of 50 keV, and an electrical current of 1.69 mA.

The XES spectra of the undoped $LuBO_3$ is shown in Figure 13. An intense emission band occurs right at the high energy edge of the investigated spectral range. This is followed by two bands, which were observed at 230 nm and 300 nm. The weak lines around 550 nm indicate Tb-impurities, and are also present in the Tb-doped sample (see Figure 13). Finally, a steady increase was detected towards longer wavelengths.

 doi:10.20944/preprints202403.0444.v1

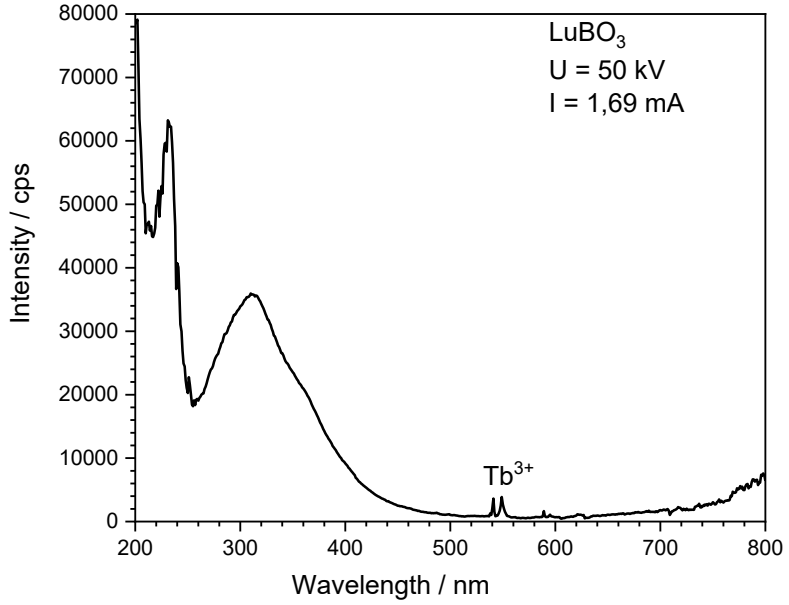

Figure 13. Emission under X-Ray excitation of the undoped $LuBO_3$ sample.

The XES spectra of the doped samples are presented in Figure 14. These show similarities to the previously shown emission spectra. First, the Ce^{3+}-doped sample (see Figure 14(a)) shows the same characteristic 5d-4f transition at the same position. The ratio of the two transitions varies notably, and the $4f5d \rightarrow {}^2F_{7/2}$ transition shows under X-ray excitation a similar intensity as the $4f5d \rightarrow {}^2F_{5/2}$ relaxation process. Further signals were observed, which were not present under the excitation with 160 nm. These are a weak band, which lies between 600 nm and 680 nm, and a sharp peak at 770 nm. The Gd^{3+} sample behaves differently as well (Figure 14(c)). The characteristic peak at 312 nm is missing, and only the band-band transition occurs. The formed excitons do not transfer the energy to the Gd since it is monovalent. The band at 330 nm was not observed as well, which appeared in the undoped sample. The relaxation via the band-band transition is either more efficient or the energy transfer is very inefficient, so that the energy is not transferred to the dopant Gd^{3+}.

In comparison, the curve of the Eu^{3+} (Figure 14(b)) and Tb^{3+} sample (Figure 14(d)) show not a significant deviation compared to excitation in the UV-range indicating the effective energy transfer to the activator in these cases. The intensities are also an order of magnitude larger than the Ce^{3+} and Gd^{3+} doped material due to the greater penetration depth of the X-rays.

 doi:10.20944/preprints202403.0444.v1

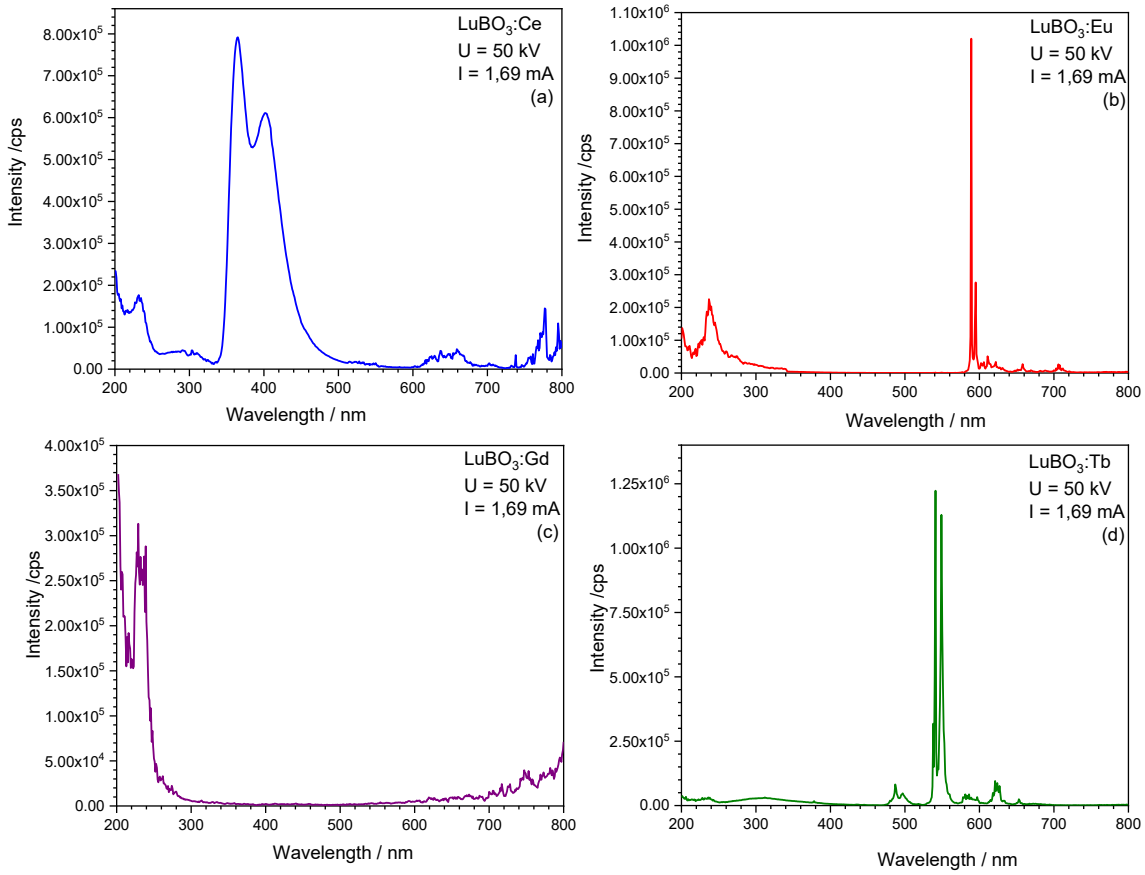

Figure 14. Emission under X-Ray excitation of (a) $LuBO_3:Ce^{3+}$, (b) $LuBO_3:Eu^{3+}$, (c) $LuBO_3:Gd^{3+}$ and (d) $LuBO_3:Tb^{3+}$.

5. Conclusions

Phase-pure $LuBO_3:RE^{3+}$ (RE=Ce^{3+}, Eu^{3+}, Gd^{3+}, Tb^{3+}) samples were prepared, that crystalized in the calcite structure. These show a large band gap, which agree with Balcerzyk's estimations. The recorder emission spectra were typically for the investigated rare earth ions, and STEs were responsible for the weak emission band in the UV-A range. Efficient scintillating properties were observed for the Ce^{3+}-, Eu^{3+}-, and Tb^{3+}-doped materials due to the efficient band excitation and charge transfer to the activator ions. $LuBO_3:Gd^{3+}$ could possibly be used as a scintillator if it is sensitized with Pr^{3+}, and thus, should be investigated.

Author Contributions: Franziska Schröder: Methodology, Investigation, Writing – original draft. **Sven Reetz:** Writing - original draft, Writing – review & editing. **Thomas Jüstel:** Supervision, Writing – review and editing, Resources.

Acknowledgments: The authors are thankful for Dr. David Enseling´s contributions to the spectroscopic measurements, and maintaining the analytical equipment.

Conflicts of Interest: The authors declare that they have no known competing financial interests or personal relationships that could have appeared to influence the work reported in this paper.

References

1. Z.-J. Zhang, T.-T. Jin, M.-M. Xu, Q.-Z. Huang, M.-R. Li, J.-T. Zhao, *Inorganic chemistry* **2015**, *54 (3)*, 969 – 975. DOI: https://doi.org/10.1021/ic502337x
2. C. Mansuy, J. M. Nedelec, C. Dujardin, R. Mahiou, *J Sol-Gel Sci Technol* **2004**, *32 (1-3)*, 253 – 258. DOI: https://doi.org/10.1007/s10971-004-5797-1
3. S. Z. Shmurak, V. V. Kedrov, A. P. Kiselev, T. N. Fursova, I. M. Smyt'ko, *Phys. Solid State* **2016**, *58 (3)*, 578 – 591. DOI: https://doi.org/10.1134/S1063783416030288

4. G. Chadeyron-Bertrand, D. Boyer, C. Dujardin, C. Mansuy, R. Mahiou, *Nuclear Instruments and Methods in Physics Research Section B: Beam Interactions with Materials and Atoms* **2005**, *229 (2)*, 232 – 239. DOI: https://doi.org/10.1016/j.nimb.2004.11.029
5. C. Mansuy, J. M. Nedelec, C. Dujardin, R. Mahiou, *Optical Materials* **2007**, *29 (6)*, 697 – 702. DOI: https://doi.org/10.1016/j.optmat.2005.10.017
6. J. Hölsä, *Inorganica Chimica Acta* **1987**, *139 (1-2)*, 257 – 259. DOI: https://doi.org/10.1016/S0020-1693(00)84089-X
7. A. Wolfert, E. Oomen, G. Blasse, *Journal of Solid State Chemistry* **1985**, *59 (3)*, 280 – 290. DOI: https://doi.org/10.1016/0022-4596(85)90295-6
8. Y. Li, J. Zhang, X. Zhang, Y. Luo, S. Lu, X. Ren, X. Wang, L. Sun, C. Yan, *Chem. Mater.* **2009**, *21 (3)*, 468 – 475. DOI: https://doi.org/10.1021/cm802015u
9. J. Yang, C. Li, X. Zhang, Z. Quan, C. Zhang, H. Li, J. Lin, *Chemistry (Weinheim an der Bergstrasse, Germany)* **2008**, *14 (14)*, 4336 – 4345. DOI: https://doi.org/10.1002/chem.200701970
10. M. Balcerzyk, Z. Gontarz, M. Moszynski, M. Kapusta, *Journal of Luminescence* **2000**, *87-89*, 963 – 966. DOI: https://doi.org/10.1016/S0022-2313(99)00492-5
11. C. Sun, X. Li, H. Wang, D. Xue, *Inorganic chemistry* **2016**, *55 (6)*, 2969 – 2976. DOI: https://doi.org/10.1021/acs.inorgchem.5b02860
12. V. Hoeke, K. Gieb, P. Müller, L. Ungur, L. F. Chibotaru, M. Heidemeier, E. Krickemeyer, A. Stammler, H. Bögge, C. Schröder, J. Schnack, T. Glaser, *Chem. Sci.* **2012**, *3 (9)*, 2868. DOI: https://doi.org/10.1039/c2sc20649h
13. Y. Gao, F. Yang, W. Han, Q. Fang, Z. Xu, *Materials Research Bulletin* **2014**, *51*, 13 – 18. DOI: https://doi.org/10.1016/j.materresbull.2013.11.037
14. J. Yang, C. Zhang, L. Wang, Z. Hou, S. Huang, H. Lian, J. Lin, *Journal of Solid State Chemistry* **2008**, *181 (10)*, 2672 – 2680. DOI: https://doi.org/10.1016/j.jssc.2008.06.045
15. L. Zhang, Y. Zhou, W. Li, X. Zhao, Y. Wang, *Chem. Pap.* **2019**, *73 (7)*, 1761 – 1766. DOI: https://doi.org/10.1007/s11696-019-00728-7
16. V. V. Mikhailin, D. A. Spassky, V. N. Kolobanov, A. A. Meotishvili, D. G. Permenov, B. I. Zadneprovski, *Radiation Measurements* **2010**, *45 (3-6)*, 307 – 310. DOI: https://doi.org/10.1016/j.radmeas.2009.12.019